






Robust Principal Component Analysis Techniques for Ground Scene Estimation in SAR Imagery

Lucas P. Ramos , *Student Member, IEEE*, Dimas I. Alves , *Member, IEEE*,
Leonardo T. Duarte , *Senior Member, IEEE*, Mats I. Pettersson , *Senior Member, IEEE*,
and Renato Machado , *Senior Member, IEEE*

Abstract—Robust principal component analysis (RPCA) has been widely used for processing and interpreting high-dimensional data in different applications such as data classification, face recognition, video analytics, and recommendation system design. However, the advancement of multisensor-based technologies and the emergence of large datasets have highlighted the limitations of traditional matrix-based models, which have paved the way for higher-order extensions such as tensor RPCA (TRPCA) techniques. These techniques can be useful for ground scene estimation (GSE) in synthetic aperture radar (SAR) imagery. GSE estimates the clutter-plus-noise content in the scene, and therefore, change detection (CD) methods can benefit, reducing the number of false alarms. This article presents two new GSE methods for SAR imagery based on robust PCA techniques. The first proposed method uses the RPCA via principal component pursuit (PCP) to obtain the GSE-RPCA. The second method uses TRPCA via new tensor nuclear norm (TNN) to obtain the GSE-TRPCA. The methodology allows the GSE to be obtained through a generalized regularization parameter. The alternating direction method of multipliers (ADMM) algorithm is utilized to solve both optimization problems. Experimental results are evaluated considering real SAR imagery from datasets acquired with the CARABAS II and ALOS PALSAR systems, respectively. Additionally, the proposed techniques were evaluated under several input characteristics, e.g., eight-image stacks and image pairs. Both GSE techniques are more robust to outliers and missing data when compared to existing solutions found in the literature. Finally, GSE-TRPCA achieved a minimum-square error performance of 0.0018 for some of the evaluated scenarios.

Index Terms—Ground scene estimation, robust principal component analysis (RPCA), SAR imagery, tensor robust principal component analysis (TRPCA).

I. INTRODUCTION

SYNTHETIC aperture radar (SAR) systems are widely used in remote sensing applications, including the mapping (or monitoring) of some terrestrial regions of interest to both civilians and military applications [1]. SAR systems are indispensable for monitoring the Earth's surface (e.g., climate forecasts [2]), environmental preservation areas (e.g., forest areas [3]) and planets in high resolution [4].

It is well known that images obtained from SAR sensors are sensitive to materials' geometric structures and dielectric properties, i.e., any significant change will produce returns at the receiver. These returns can be mainly associated with targets, i.e., objects of interest to the application, such as military vehicles hidden in forests, oil platforms, and illegal runways. There are also returns relating to the acquisition environment, such as ground, sea, and buildings. These returns are generally known as clutter. Furthermore, the SAR image is strongly affected by noise, related to the image acquisition process [1]. Removing the clutter-plus-noise in the SAR image can be a challenge for change detection (CD) methods (i.e., methods that aim to detect targets that emerge over time [5], [6], [7]), since the spectral characteristics, especially of the clutter, are often similar to those of the target. [8].

To deal with that, ground scene estimation (GSE) methods can be an interesting approach, as this type of method allows an estimate of the clutter-plus-noise content of the SAR image. From an accurate GSE, i.e., the clutter-plus-noise content without the presence of targets, CD methods can obtain a better performance. In these methods, the reference image is generally used to suppress the clutter-plus-noise content of the surveillance image. If there are targets in the reference image, the targets in the surveillance image tend to be suppressed. Recently, Ramos et al. [9] showed the performance of the CD method improved when a GSE [10] scheme is used as reference image input [11]. In addition, Alves et al. [12] showed that more accurate clutter-plus-noise statistics reduce FA in an iterative CD method, consequently achieving better performance. Thus, GSE methods become even more important as they can enhance CD methods.

Manuscript received 23 August 2023; revised 29 September 2023; accepted 10 October 2023. Date of publication 16 October 2023; date of current version 25 October 2023. This work was supported in part by the Brazilian Agencies National Council for Scientific and Technological Development (CNPq), in part by the Ministry of Science, Technology and Innovation (MCTI), in part by the Swedish-Brazilian Research and Innovation Centre (CISB), Saab AB, in part by the Coordination for the Improvement of Higher Education Personnel (CAPES)—Finance Code 001 (PróDefesa IV), and in part by São Paulo Research Foundation (FAPESP) under Grant 2020/09838-0 (BIOS—Brazilian Institute of Data Science). (Corresponding author: Lucas P. Ramos.)

Lucas P. Ramos is with the Department of Telecommunications, Aeronautics Institute of Technology, São José dos Campos 12228-900, Brazil, and also with the Department of Mathematics and Natural Sciences, Blekinge Institute of Technology, 371 79 Karlskrona, Sweden (e-mail: lucaspr@ita.br).

Dimas I. Alves and Renato Machado are with the Department of Telecommunications, Aeronautics Institute of Technology, São José dos Campos 12228-900, Brazil (e-mail: dimasirion@ita.br; rmachado@ita.br).

Leonardo T. Duarte is with the School of Applied Sciences, University of Campinas, Limeira 13484-350, Brazil (e-mail: leonardo.duarte@fca.unicamp.br).

Mats I. Pettersson is with the Department of Mathematics and Natural Sciences, Blekinge Institute of Technology, 371 79 Karlskrona, Sweden (e-mail: mats.pettersson@bth.se).

Digital Object Identifier 10.1109/JSTARS.2023.3324732

Since different sources contribute to the formation of the SAR image, such as clutter, noise, and targets, it is difficult for nonrobust methods to estimate the GSE. Different approaches seek to estimate the ground scene in SAR imagery [13], [14]. Some methods aim to characterize the amplitude values of image pixels through statistical analysis, and most of them require a priori information about the target or clutter [15], [16], [17]. Palm et al. [18] proposed a preliminary study considering a GSE based on a single wavelength-resolution (WR) SAR image stack using an autoregressive model. However, using a time series model may not be suitable for GSE since the noise in the image stack is not correlated over time. Recently, Palm et al. [10] proposed a GSE based on measures of central trends such as mean, median, and trimmed mean considering WR image stacks. Significant drawbacks of approaches based on those measures include sensitivity to noise, missing data, and dependence on the number of images in the stack.

An efficient strategy to face these issues is through robust principal component analysis (RPCA) techniques, which have stood out as a source separation method in different applications such as biomedical engineering, telecommunications, and financial data [19], [20]. The most representative formulation of RPCA, known as principal component pursuit (PCP) [21], seeks to decompose the input matrix into a low-rank background matrix (highly coherent) and a sparse matrix that is associated with a disturbance or outliers [22]. However, there are currently other formulations of RPCA. Such formulations differ in the loss functions, optimization problems, or even the solution methods adopted [22], [23]. In SAR imaging applications, different authors seek to use a relaxed version of the PCP in the context of ground moving-target indication (GMTI) [24], [25], [26]. Schwartz et al. [27] and Ramos et al. [28] explored the multitemporal diversity of the WR SAR images through RPCA via PCP, aiming to detect stationary military vehicles hidden under the forest. Furthermore, Gong et al. [29] showed that RPCA could work as a preprocessing tool in change detection applications, separating irrelevant features and noise from the SAR image.

Since RPCA looks for the lowest rank of the input matrix, vectorizing the images becomes an interesting strategy to explore the temporal diversity of the data, as is the interest of change detection applications [27], [30]. However, the vectorization causes a loss of spatial information since the analysis is done pixel by pixel. In SAR imagery, exploring spatial information is interesting since this information is usually related to the same target or background content. In the face of that, many recent studies extended the RPCA matrix problem to tensors RPCA (TRPCA) by taking advantage of the multidimensional structure of the data [31], [32], [33], [34]. For example, Lu et al. [35] proposed a TRPCA problem based on a new tensor nuclear norm (TNN) which is induced by the tensor-tensor product (T-product). Such generalization showed that it is possible to perfectly recover the sparse and low-rank tensor with much better performance than the matrix-based RPCA in optical image recovery applications and background modeling problems [35].

Currently, there is a need for more robust methods to obtain the GSE in SAR images. The main challenge is obtaining the GSE without the presence of targets, which is usually presented

in the SAR imagery. We propose using robust PCA techniques based on RPCA and TRPCA for GSE in SAR imagery. The first proposed method uses the RPCA via PCP to obtain the GSE. In this method, the input SAR images are concatenated into a matrix of size (number of images, number of rows \times number of columns), allowing us to obtain the low-rank matrix, i.e., the GSE-RPCA. The second method uses TRPCA via TNN to obtain the GSE. In this method, the input SAR images are organized into a third-order tensor of size (number of images, number of rows, number of columns), allowing to obtain the low-rank tensor, i.e., the GSE-TRPCA. To solve both problems, we use the polynomial-time algorithm known as the alternating direction method of multiplier (ADMM), which is the most widely used solver for RPCA and its related problems [32].

The GSE scheme proposed was first evaluated in real WR SAR images obtained with Coherent All Radio Band System II (CARABAS-II), a Swedish ultrawideband (UWB) very-high frequency (VHF) SAR system. Furthermore, the GSE scheme was evaluated in polarimetric SAR images obtained with the advanced land observing satellite (ALOS) phased arrayed L-band synthetic aperture radar (PALSAR) system, a Japanese SAR system operating at L-band. Thus, the GSE scheme proved to work for different applications. In summary, the major contributions are listed as follows.

- 1) Our GSE in SAR imagery performs better than existing methods in the literature.
- 2) The proposed scheme does not depend on the presence of SAR image stacks, which can often limit the application of other methods, as obtaining many SAR images is usually expensive.
- 3) The GSE obtained is not sensitive to outliers and missing data, as are traditional methods based on statistical measures of central tendency.
- 4) Even generating a GSE for each image of the stack in both methods, the GSE-RPCA method showed that obtaining a single clutter-plus-noise image is possible since all GSE-RPCA are linearly dependent.
- 5) Our methodology shows that obtaining different GSEs based on RPCA or TRPCA is possible from a single regularization parameter.

The rest of this article is organized as follows. Section II presents the considered data and its characteristics. In Sections III-A and III-B, RPCA via PCP and TRPCA via TNN are described, respectively. Then, the methodology and implementation aspects are presented in Section III-C. Sections IV-A and IV-B present and discuss the results considering data referring to the CARABAS-II and PALSAR systems, respectively. Section IV-C presents a brief discussion about the characteristics of the GSE obtained. Finally, Section V concludes the article.

II. DATASETS

The proposed GSE method was tested on two real multitemporal SAR datasets. Initially, we evaluated the method with real WR data (VHF-band, HH-polarization) obtained by the Swedish Airborne CARABAS-II SAR system. The second dataset consists of polarimetric SAR images (L-band, HH-polarization)

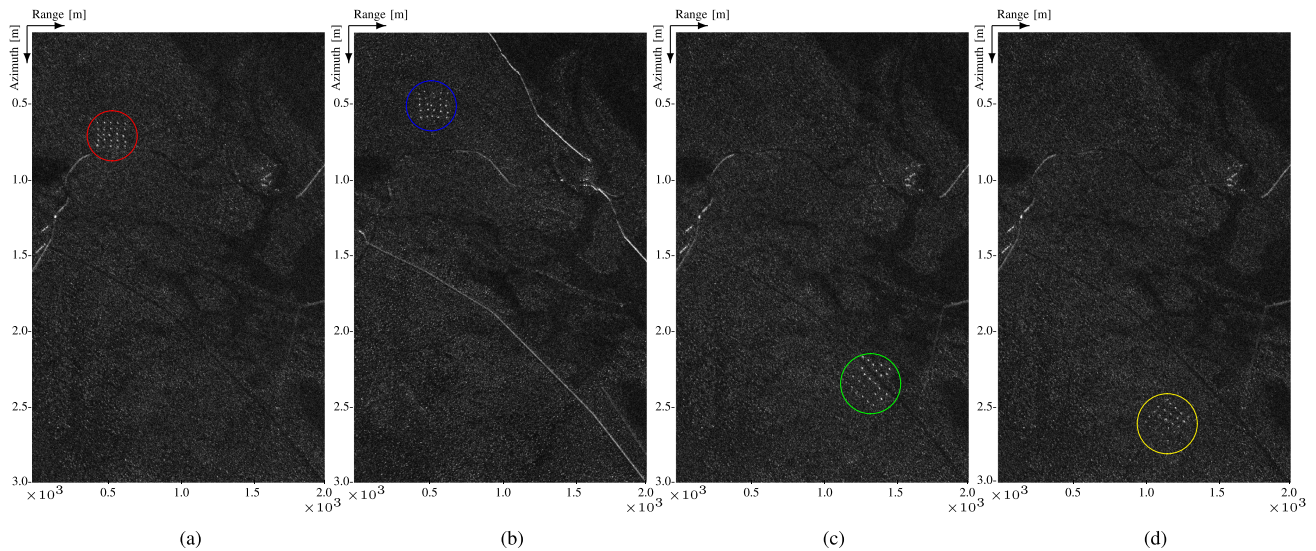


Fig. 1. Example of magnitude HH-polarized SAR images from the CARABAS-II dataset: (a) Mission 1, Pass 1 (225° , Stack 1); (b) Mission 2, Pass 2 (135° , Stack 2); (c) Mission 3, Pass 6 (230° , Stack 3); and (d) Mission 4, Pass 6 (230° , Stack 3). The circles show military vehicles deployed in each mission.

TABLE I
CARABAS-II IMAGES ORGANIZED IN STACKS

Data	N	Flight Heading	Pass	Mission
Stack 1	8	225°	1 and 3	1,2,3, and 4
Stack 2	8	135°	2 and 4	1,2,3, and 4
Stack 3	8	230°	5 and 6	1,2,3, and 4

obtained from the ALOS PALSAR system. Next, it presents the two datasets.

A. CARABAS-II Data

CARABAS-II is a VHF UWB SAR system projected by Swedish National Defence Research Establishment (FOA). It operates in the 20–90 MHz band and provides imagery with a spatial resolution in the order of 2.5 m in both azimuth and range dimensions [36]. In this frequency range, mainly in the lower VHF, the wavelength of the system is relatively long, and, therefore, most objects referring to biomass (e.g., foliage and branches) are in the Rayleigh scattering regime. In this context, the ability of objects to reflect signals toward the system receiver is considerably attenuated, allowing penetration into the vegetation. On the other hand, objects in the order of the radar signal wavelength (e.g., buildings and vehicles) contribute significantly to the radar signature, making this system suitable for detecting targets hidden by biomass and stealth-designed human-made objects [6], [37], [38]. Due to the resolution of the system being in the order of the radar signal wavelength, such systems are named WR SAR systems [39].

In this study, we consider a CARABAS-II data set from the measurement campaign in northern Sweden in 2002 [40], which was made publicly available by U.S. Air Force Research Laboratory (AFRL) at the sensor data management system (SDMS) website [41]. The dataset is formed by 24 magnitude WR SAR images (calibrated, preprocessed, and geocoded) characterized by forested areas, lakes, human-made structures, roads, and

transmission lines in an area of 6 km^2 ($3 \text{ km} \times 2 \text{ km}$). Since the image sample is $1 \text{ m} \times 1 \text{ m}$, each image can be represented by a matrix of 3000×2000 pixels (rows \times columns).

The dataset is divided into four missions (named Mission 1, 2, 3, and 4), where each mission corresponds to the deployment of 25 military vehicles at a certain location in the SAR scene. Each mission consists of six platform passes marked by the numbers 1–6, where two passes are made with a flight heading of 225° (Pass 1 and 3), two with a flight heading of 135° (Pass 2 and 4), and two with a flight heading of 230° (Pass 5 and 6). In this context, the heading is set to 0° pointing north with increasing heading clockwise [40].

To evaluate the proposed method, WR SAR images are grouped into different stacks. Each stack is formed by images with the same flight heading. It is possible to obtain three stacks with a maximum of eight images, as shown in Table I. Fig. 1 shows examples of WR SAR images from different missions and different flight headings. It can be seen that the targets (military vehicles) in Missions 1 and 2 are presented in the upper-left region, while in Missions 3 and 4, the targets are presented in the lower-right region.

B. ALOS PALSAR Data

The ALOS PALSAR system was launched in January of 2006 by the Japan Aerospace Exploration Agency (JAXA), aiming to contribute to the fields of mapping, precise regional land-coverage observation, disaster monitoring, and resource surveying [42]. In 2016, global mosaics of ALOS PALSAR HH and HV polarization data at 25 m spatial resolution and forest/nonforest maps were released by JAXA using data acquired annually from 2007 to 2010 [43]. The datasets are freely available to the public on the ALOS website [44].

Fig. 2 presents a sample of backscatter (σ°) SAR images in polarizations HH and HV and the forest mapping from the PALSAR mosaic collected over a port region in southern Brazil

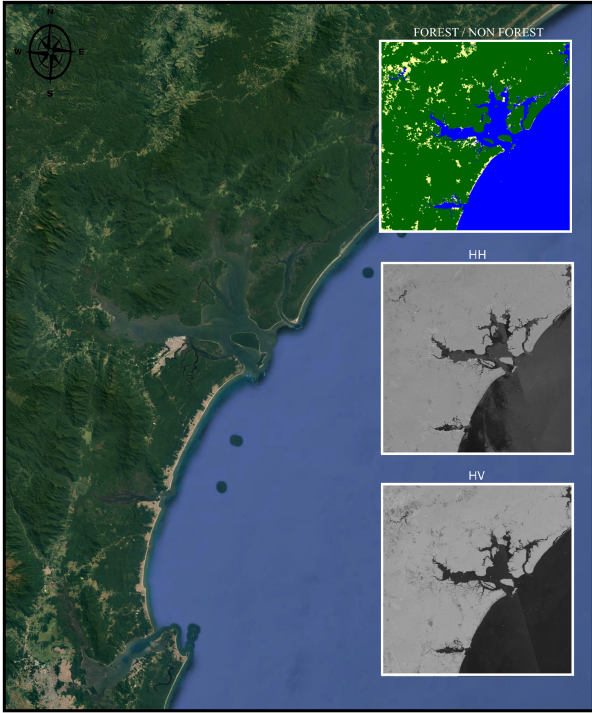


Fig. 2. Polarimetric and Forest/nonforest PALSAR images collected in 2007 over the Paranaguá port in Brazil.

in 2007. As background, the same region can be observed from a mapping generated by Google Earth in 2022. More details on preprocessing steps, mosaic generation, and radiometric and geometric calibration of the polarimetric PALSAR images can be found in [43], [44], and [45].

In this study, we considered four σ° PALSAR images (one image for each year) in the HH polarization, as shown in Fig. 3. Each image is given as a 3000×2000 matrix and refers to the region shown in Fig. 2. This region is characterized by the presence of the Paranaguá port ($25^\circ 30' S$, $48^\circ 31' W$), forest, buildings, and ships in the ocean. Paranaguá port is one of the largest exporting ports of agricultural products in Brazil.

III. METHODS AND METHODOLOGY

Principal component analysis (PCA) is a low-rank matrix factorization method validated as a powerful tool for processing and interpreting high-dimensional data in different applications such as data classification, face recognition, video analytics, and recommendation system design [46], [47], [48]. The problem addressed by PCA can be defined as the orthogonal projection that minimizes the mean square error between the original data, $\mathbf{X} \in \mathbb{R}^{n_1 \times n_2}$, and its low-rank approximation, $\mathbf{L} \in \mathbb{R}^{n_1 \times n_2}$ [49]. In this context, the optimal low-rank approximation of \mathbf{X} can be obtained by solving the following optimization problem:

$$\begin{aligned} & \text{minimize} \quad \|\mathbf{X} - \mathbf{L}\|_F^2 \\ & \text{subject to} \quad \text{rank}(\mathbf{L}) \leq l \end{aligned} \quad (1)$$

where $\|\cdot\|_F$ denote the Frobenius norm. This optimization problem has the constraint that $\text{rank}(\mathbf{L})$ must be at most k , which is usually fewer than $\text{rank}(\mathbf{X})$.

In this approach, PCA can be seen as the Frobenius norm minimization of an \mathbf{N}_0 noise term, where $\mathbf{X} = \mathbf{L} + \mathbf{N}_0$. Due to this formulation, it is observed that PCA is sensitive to outliers, in which its performance is significantly reduced even in the face of a few corrupted samples [50]. Furthermore, a single outlier, i.e., peak value, can cause the main components to be distorted to fit the outlier, resulting in an inadequate interpretation of the results [51]. The applicability of PCA is thus limited in our scenarios.

In theory, classical PCA could be used for decomposing the images into different subimages. However, PCA, as shown in many works in the field of source separation [52], is not appropriate for performing signal separation. In fact, PCA uniquely assumes that the retrieved components (in our case, desired sources) are uncorrelated, and such an assumption is usually not enough to ensure signal separation. To sum up, the application of classical PCA, in this case, would be adapted to problems such as feature extraction preceding classification tasks and data compression [46].

A. Robust PCA

In recent years, there has been a need to deal with relatively large and corrupted data by outliers in research areas such as image processing, computer vision, machine learning, and bioinformatics. Therefore, techniques to give robustness to PCA have become increasingly important [46]. The most popular among those is the idea of decomposing a given data \mathbf{X} as follows:

$$\mathbf{X} = \mathbf{L} + \mathbf{S} \quad (2)$$

where $\mathbf{S} \in \mathbb{R}^{n_1 \times n_2}$ is a sparse matrix (representing outliers) [22].

Since the number of unknowns to be inferred in \mathbf{L} and \mathbf{S} is twice the number of unknowns in \mathbf{X} , this problem seems ill-posed at first sight. However, Candès et al. [21] showed that it is possible to recover a low-rank matrix \mathbf{L} with errors in \mathbf{S} of arbitrarily large values through a formulation known as PCP. PCP seeks to solve the convex optimization problem which is given by

$$\begin{aligned} & \text{minimize} \quad \|\mathbf{L}\|_* + \lambda_{\text{RPCA}} \|\mathbf{S}\|_1 \\ & \text{subject to} \quad \mathbf{L} + \mathbf{S} = \mathbf{X} \end{aligned} \quad (3)$$

where $\|\mathbf{L}\|_* = \sum_i \sigma_i(\mathbf{X})$ represents the nuclear norm of \mathbf{L} (i.e., the sum of singular values, σ_i) as a low-rank approximation, $\|\mathbf{S}\|_1 = \sum_{i,j} |\mathbf{X}_{ij}|$ represents the norm l_1 (i.e., the sum of absolute values of the entries) as a heuristic to find sparse representations, and $\lambda_{\text{RPCA}} > 0$ is a regularization parameter which allows an interesting tradeoff analysis, balancing the content between \mathbf{L} and \mathbf{S} [21].

Through this convex problem, PCP converges to a decomposition that minimizes the weighted combination between the nuclear norm and the l_1 norm at a computational cost that is not much higher than the classical PCA. Content separation is

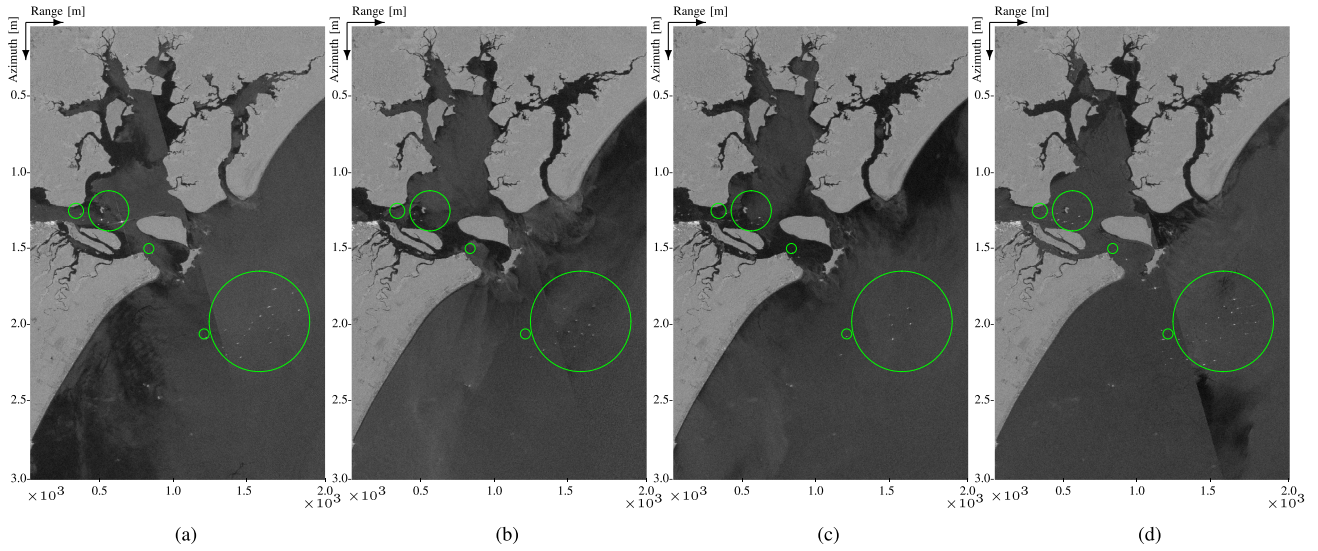


Fig. 3. Example of σ° HH-polarization SAR images from the ALOS PALSAR data: (a) 2007; (b) 2008; (c) 2009; and (d) 2010. The circles show selected ships that can be viewed.

performed during iterations of the algorithm until reaching a certain measure of sparsity for \mathbf{S} . This sparsity value depends on the choice of λ_{RPCA} . According to [21], a good choice is defining λ_{RPCA} as

$$\lambda_{\text{RPCA}} = \frac{1}{\sqrt{\max(n_1, n_2)}} \quad (4)$$

where n_1 and n_2 denote the number of rows and columns of the \mathbf{X} input matrix, respectively.

There are different ways to solve the optimization problem presented in (3). Many of these methods are usually based on the augmented Lagrange multiplier (ALM) method or its variants [20], [53], [54]. For the RPCA via PCP problem, the augmented Lagrangian function (L) is defined as follows:

$$L(\mathbf{L}, \mathbf{S}, \Lambda, \mu) \doteq \|\mathbf{L}\|_* + \lambda_{\text{RPCA}} \|\mathbf{S}\|_1 + \langle \Lambda, \mathbf{X} - \mathbf{L} - \mathbf{S} \rangle + \frac{\mu}{2} \|\mathbf{X} - \mathbf{L} - \mathbf{S}\|_F^2 \quad (5)$$

where Λ represents the Lagrange multiplier matrix, $\mu > 0$ denotes the incoherence parameter, and the Euclidean inner product between two matrices A and B is defined as $\langle A, B \rangle = \text{trace}(A^* B)$. At each iteration, the classical ALM seeks to solve the following subproblems:

$$\begin{cases} \mathbf{L}^{(t+1)}, \mathbf{S}^{(t+1)} = \arg \min_{\mathbf{L}, \mathbf{S}} L(\mathbf{L}, \mathbf{S}, \Lambda^{(t)}), \\ \Lambda^{(t+1)} = \Lambda^{(t)} + \mu (\mathbf{L}^{(t+1)} + \mathbf{S}^{(t+1)} - \mathbf{X}). \end{cases} \quad (6)$$

The ALM approach consists of a joint optimization between the variables \mathbf{L} and \mathbf{S} . This shows that the classical ALM considers PCP as a generic problem and ignores its separable structure [55]. One way to deal with the problem is through the ADMM. The ADMM performs the optimization alternately, splitting the minimization problem into two smaller and simpler sub-problems. Thus, the ADMM method seeks to solve the

following subproblems:

$$\begin{cases} \mathbf{L}^{(t+1)} = \arg \min_{\mathbf{L}} L(\mathbf{L}, \mathbf{S}^{(t)}, \Lambda^{(t)}), \\ \mathbf{S}^{(t+1)} = \arg \min_{\mathbf{S}} L(\mathbf{L}^{(t+1)}, \mathbf{S}, \Lambda^{(t)}), \\ \Lambda^{(t+1)} = \Lambda^{(t)} + \mu (\mathbf{L}^{(t+1)} + \mathbf{S}^{(t+1)} - \mathbf{X}). \end{cases} \quad (7)$$

The ADMM method can be written by combining the linear and quadratic terms of the augmented Lagrangian function. In addition, a stepsize ρ can be considered to increase μ to μ_{max} aiming to improve the convergence rate of the method as suggested in [56]. Thus, we can rewrite (7) as

$$\begin{cases} \mathbf{L}^{(t+1)} = \arg \min_{\mathbf{L}} \left\{ \|\mathbf{L}\|_* + \frac{\mu^{(t)}}{2} \left\| \mathbf{L} + \mathbf{S}^{(t)} - \mathbf{X} + \frac{\Lambda^{(t)}}{\mu^{(t)}} \right\|_F^2 \right\}, \\ \mathbf{S}^{(t+1)} = \arg \min_{\mathbf{S}} \left\{ \|\mathbf{S}\|_1 + \frac{\mu^{(t)}}{2} \left\| \mathbf{L}^{(t+1)} + \mathbf{S} - \mathbf{X} + \frac{\Lambda^{(t)}}{\mu^{(t)}} \right\|_F^2 \right\}, \\ \Lambda^{(t+1)} = \Lambda^{(t)} + \mu^{(t)} (\mathbf{L}^{(t+1)} + \mathbf{S}^{(t+1)} - \mathbf{X}), \\ \mu^{(t+1)} = \min(\rho \mu^{(t)}, \mu_{\text{max}}). \end{cases} \quad (8)$$

Initially, the idea of the ADMM method is to minimize the Lagrangian function according to \mathbf{L} while keeping \mathbf{S} fixed. The next step is to minimize \mathbf{S} keeping \mathbf{L} fixed and finally Λ and μ are updated as the residue $(\mathbf{X} - \mathbf{L} - \mathbf{S})$ and the stepsize, respectively. The idea above is summarized in Algorithm 1. According to [21] and [57], these steps can be solved simply by defining the soft-thresholding operator (\mathcal{E}_k) and the singular value thresholding operator (\mathcal{D}_k) as

$$\mathcal{E}_k(x) = \text{sgn}(x) \max(|x| - k, 0), \quad (9)$$

$$\mathcal{D}_k(X) = U \mathcal{E}_k(\Sigma) V^*, \quad (10)$$

$$X = U \Sigma V^*. \quad (11)$$

Algorithm 1: Solve (3) by ADMM [55].

Input: $\mathbf{X}, \mathbf{L}^{(0)} = \mathbf{S}^{(0)} = \Lambda^{(0)} = 0,$
 $\rho > 1, \mu_{max} \geq \mu^0 > 0.$
Output: $\mathbf{L}, \mathbf{S}.$
repeat

$$\mathbf{L}^{(t+1)} = \mathcal{D}_{\frac{1}{\mu^{(t)}}}(\mathbf{X} - \mathbf{S}^{(t)} + \frac{\Lambda^{(t)}}{\mu^{(t)}});$$

$$\mathbf{S}^{(t+1)} = \mathcal{E}_{\frac{\lambda_{RPCA}}{\mu^{(t)}}}(\mathbf{X} - \mathbf{L}^{(t+1)} + \frac{\Lambda^{(t)}}{\mu^{(t)}});$$

$$\Lambda^{(t+1)} = \Lambda^{(t)} + \mu^{(t)}(\mathbf{S}^{(t+1)} + \mathbf{L}^{(t+1)} - \mathbf{X}).$$

$$\mu^{(t+1)} = \min(\rho\mu^{(t)}, \mu_{max}).$$

until the convergence criterion is met.

B. Tensor Robust PCA

It is known that approaches based on matrix (i.e., 2-D array) signal separation are efficient tools for different applications such as BSS, feature extraction, or even classification of datasets [58], [59]. However, the advancement of multisensor-based technologies and the emergence of large datasets have highlighted the limitations of traditional matrix-based models. Thus, more versatile data analysis tools, such as higher-order tensors (i.e., multidimensional arrays) strategies, are encouraged [60].

Tensor-based strategies have several advantages over matrix-based methods ranging from the uniqueness of the optimal solution to component identification, even when most data is missing. One of the main advantages of using tensors is to exploit the multidimensional structure of the data. In fact, this information is often lost in matrix-based strategies and can degrade the performance of the method [61].

Recently, Lu et al. [35] proposed to extend the RPCA matrix problem (i.e., $\mathbf{X} \in \mathbb{R}^{n_1 \times n_2}$) to third-order tensors $\mathcal{X} \in \mathbb{R}^{n_1 \times n_2 \times n_3}$, where n_1 , n_2 , and n_3 represents the horizontal, lateral, and frontal slice of the tensor, respectively. The method known as TRPCA seeks to decompose a given tensor \mathcal{X} as

$$\mathcal{X} = \mathcal{L} + \mathcal{S} \quad (12)$$

where $\mathcal{L} \in \mathbb{R}^{n_1 \times n_2 \times n_3}$ is a low-rank tensor, and $\mathcal{S} \in \mathbb{R}^{n_1 \times n_2 \times n_3}$ is a sparse tensor.

In this context, [35] has proven that it is possible to perfectly obtain \mathcal{L} and \mathcal{S} with a tight recovery guarantee similar to that of the matrix RPCA through the following optimization problem:

$$\begin{aligned} & \text{minimize } \|\mathcal{L}\|_* + \lambda_{TRPCA} \|\mathcal{S}\|_1 \\ & \text{subject to } \mathcal{L} + \mathcal{S} = \mathcal{X} \end{aligned} \quad (13)$$

where $\|\mathcal{L}\|_*$ is the tensor nuclear norm of \mathcal{L} , which can be computed by the sum of singular values of all the frontal slices of \mathcal{L} , i.e., $\|\mathcal{L}\|_* := \sum_{i=1}^{n_3} \|\bar{\mathbf{L}}^{(i)}\|_*$, where $\bar{\mathbf{L}}^{(i)}$ is the i th frontal slice of \mathcal{L} , and $\bar{\mathcal{L}} = \text{fft}(\mathcal{L}, [], 3)$ [35], [62], [63]. The tensor nuclear norm is induced by transforms-based tensor-tensor product (T-product) [64], which is a generalization of the matrix-matrix product. More details on the tensor nuclear norm can be found in [32]. In addition, the sparse content is computed by summing the absolute values of all entries in \mathcal{S} with λ_{TRPCA} balancing the content between \mathcal{L} and \mathcal{S} . According to [35], the λ_{TRPCA} value

Algorithm 2: Solve (13) by ADMM.

Input: $\mathcal{X}, \mathcal{L}^{(0)} = \mathcal{S}^{(0)} = \mathcal{Y}^{(0)} = 0,$
 $\rho > 1, \mu_{max} \geq \mu^0 > 0.$
Output: \mathcal{L}, \mathcal{S}
repeat

$$\mathcal{L}^{(t+1)} = \mathcal{T}_{\frac{1}{\mu^{(t)}}}(\mathcal{X} - \mathcal{S}^{(t)} + \frac{\mathcal{Y}^{(t)}}{\mu^{(t)}});$$

$$\mathcal{S}^{(t+1)} = \mathcal{E}_{\frac{\lambda_{TRPCA}}{\mu^{(t)}}}(\mathcal{X} - \mathcal{L}^{(t+1)} + \frac{\mathcal{Y}^{(t)}}{\mu^{(t)}});$$

$$\mathcal{Y}^{(t+1)} = \mathcal{Y}^{(t)} + \mu^{(t)}(\mathcal{S}^{(t+1)} + \mathcal{L}^{(t+1)} - \mathcal{X});$$

$$\mu^{(t+1)} = \min(\rho\mu^{(t)}, \mu_{max}).$$

until the convergence criterion is met.

that exactly recovers \mathcal{L}_0 and \mathcal{S}_0 under certain assumptions is defined by

$$\lambda_{TRPCA} = \frac{1}{\sqrt{\max(n_1, n_2) \times n_3}}. \quad (14)$$

It is interesting to note that for $n_3 = 1$, $\lambda_{TRPCA} = \lambda_{RPCA}$. For this special case, the TRPCA model (13) reduces to the RPCA model (Section III-A) with the same recovery guarantee as [21].

Similar to the RPCA model, the TRPCA problem can be solved by polynomial-time algorithms through the ADMM method. Thus, (13) solved by ADMM consists of the following iterations:

$$\begin{aligned} L(\mathcal{L}, \mathcal{S}, \mathcal{Y}, \mu) & \doteq \|\mathcal{L}\|_* + \lambda_{TRPCA} \|\mathcal{S}\|_1 \\ & + \langle \mathcal{Y}, \mathcal{X} - \mathcal{L} - \mathcal{S} \rangle + \frac{\mu}{2} \|\mathcal{X} - \mathcal{L} - \mathcal{S}\|_F^2 \end{aligned} \quad (15)$$

where \mathcal{Y} represents the Lagrange multiplier tensor [35]. Then, (15) can be alternatively optimized over one variable while fixing the others [65]. As result, the TRPCA problem is decomposed into subproblems as follows:

$$\begin{cases} \mathcal{L}^{(t+1)} = \arg \min_{\mathcal{L}} \left\{ \|\mathcal{L}\|_* + \frac{\mu^{(t)}}{2} \left\| \mathcal{L} + \mathcal{S}^{(t)} - \mathcal{X} + \frac{\mathcal{Y}^{(t)}}{\mu^{(t)}} \right\|_F^2 \right\}, \\ \mathcal{S}^{(t+1)} = \arg \min_{\mathcal{S}} \left\{ \|\mathcal{S}\|_1 + \frac{\mu^{(t)}}{2} \left\| \mathcal{L}^{(t+1)} + \mathcal{S}^{(t)} - \mathcal{X} + \frac{\mathcal{Y}^{(t)}}{\mu^{(t)}} \right\|_F^2 \right\}, \\ \mathcal{Y}^{(t+1)} = \mathcal{Y}^{(t)} + \mu^{(t)} (\mathcal{L}^{(t+1)} + \mathcal{S}^{(t+1)} - \mathcal{X}), \\ \mu^{(t+1)} = \min(\rho\mu^{(t)}, \mu_{max}). \end{cases} \quad (16)$$

Details of the optimization can be seen in Algorithm 2. Note that the key step of the algorithm is to compute the tensor singular value thresholding operator (\mathcal{T}_k), which can be performed on the frontal slices of the tensor in the Fourier domain (See Algorithm 3 in [35] for more details).

C. Methodology

This section presents the proposed method in detail. Fig. 4 shows the general diagram of the proposed method. Initially, we consider \mathbf{I} as the SAR image stack, which is used for obtaining the GSE. \mathbf{I} is formed by $I_N \in \mathbb{R}^{n \times m}$, where N is the number of images in the stack, n , and m represents the rows and columns

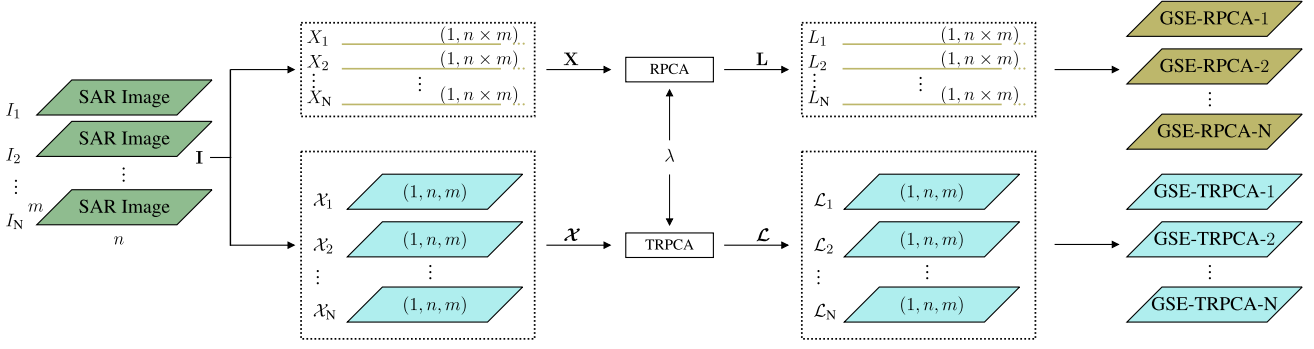


Fig. 4. Simplified diagram for GSE in SAR imagery based on RPCA and TRPCA.

of each image, respectively. Before applying the techniques, it is necessary to organize the stack accordingly to obtain either \mathbf{X} (for RPCA) and \mathcal{X} (for TRPCA).

Let \mathbf{X} be the matrix formed by X_1, X_2, \dots, X_N vectors, which X_N represents the concatenation of the image I_N . Thus, the dimension of \mathbf{X} is $(N, n \times m)$. Considering that $\mathbf{X} \in \mathbb{R}^{N, n \times m}$ and $n \times m \gg N$, λ_{RPCA} (4) can be approximated by

$$\lambda_{\text{RPCA}} = \frac{1}{\sqrt{\max(N, n \times m)}} = \frac{1}{\sqrt{n \times m}}. \quad (17)$$

According to the definition of tensors [60], the SAR image stack can be represented as a third-order tensor $\mathcal{X} \in \mathbb{R}^{N \times n \times m}$. From this arrangement and considering $n \gg N$, λ_{TRPCA} (14) is given by

$$\lambda_{\text{TRPCA}} = \frac{1}{\sqrt{\max(N, n) \times m}} = \frac{1}{\sqrt{n \times m}}. \quad (18)$$

We can observe that $\lambda_{\text{TRPCA}} = \lambda_{\text{RPCA}} = \lambda$. Thus, the methodology allows obtaining the GSE from a generalized λ value, which depends only on the size of the SAR image. Considering the 3000×2000 -sized SAR images presented in Section II, λ is equal to 4.0825×10^{-4} . Furthermore, other parameters must be defined to obtain the GSE. Following the MATLAB implementations of the RPCA via PCP [66] and the TRPCA via TNN [67], methods are initialized with $\mu^0 = 10 \times \lambda$, $\mu_{\text{max}} = 10^{10}$, $\rho = 1.1$. As stopping criteria, we consider an error (ξ) equal to 10^{-6} and 500 iterations for both methods. Similar to [21] and [66], ξ in the GSE-RPCA method is taken from

$$\frac{\|\mathbf{X} - \mathbf{L}^t - \mathbf{S}^t\|_F}{\|\mathbf{X}\|_F}. \quad (19)$$

As suggested in [35] and [67], ξ in the GSE-TRPCA method is taken from

$$\|\mathcal{L}^{t+1} - \mathcal{L}^t\|_{\infty}, \quad (20)$$

$$\|\mathcal{S}^{t+1} - \mathcal{S}^t\|_{\infty}, \quad (21)$$

$$\|\mathcal{L}^{t+1} + \mathcal{S}^{t+1} - \mathcal{X}\|_{\infty} \quad (22)$$

where $\|\cdot\|_{\infty}$ represents the infinite norm, and the stop criterion is attended when (20) or (21) or (22) converges to the ξ value.

IV. EXPERIMENTAL RESULTS AND ANALYSIS

This section presents the GSE results based on RPCA and TRPCA using the images presented in Section II. The GSE method is evaluated by considering stacks ($N = 8$) and pairs ($N = 2$) of WR SAR images and a stack ($N = 4$) of PALSAR images.

A. GSE Results on WR SAR Images

To demonstrate the effectiveness of the GSE method, visual and quantitative comparisons are made with the results obtained in [10], which, to the best of our knowledge, is the work that presents the best performance related to GSE in WR SAR image stacks using the CARABAS II dataset. To make a fair comparison, we used exactly the image stacks (see Table I) and metrics that have been considered in [18] and [10]. Also, we evaluate our method through the same interest image used in [18] and [10]. The interest image is an original image chosen for analysis. Therefore, the interest image has targets. In this context, Stacks 1, 2, and 3 are evaluated by interest images from Mission 1, Pass 1, 2, and 5, respectively. We also limited our GSE quantitative analysis to Mission 1, which is representative of all missions due to WR SAR image stability as suggested in [10] (more details can be found in [68]).

Initially, the GSE can be evaluated visually. Figs. 5 and 6 show the GSE-RPCA and GSE-TRPCA, respectively, using a WR SAR images with $N = 8$. In this case, it was possible to remove all targets from Mission 1 [see Azimuth 500–1000 in Fig. 1(a)] using the proposed method. In addition, the GSE provided information regarding linear objects such as fences and power lines, which significantly contributes to reducing false alarms in change detection algorithms.

We evaluate the GSE in terms of statistical measures such as average (\bar{x}), standard deviation (σ), skewness (μ_3 , measure of the asymmetry of a distribution), and kurtosis (μ_4 , measure of tailedness of a distribution) [69], [70]. These measures are defined by

$$\bar{x} = \frac{1}{Q} \sum_{i=1}^Q x[q], \quad (23)$$

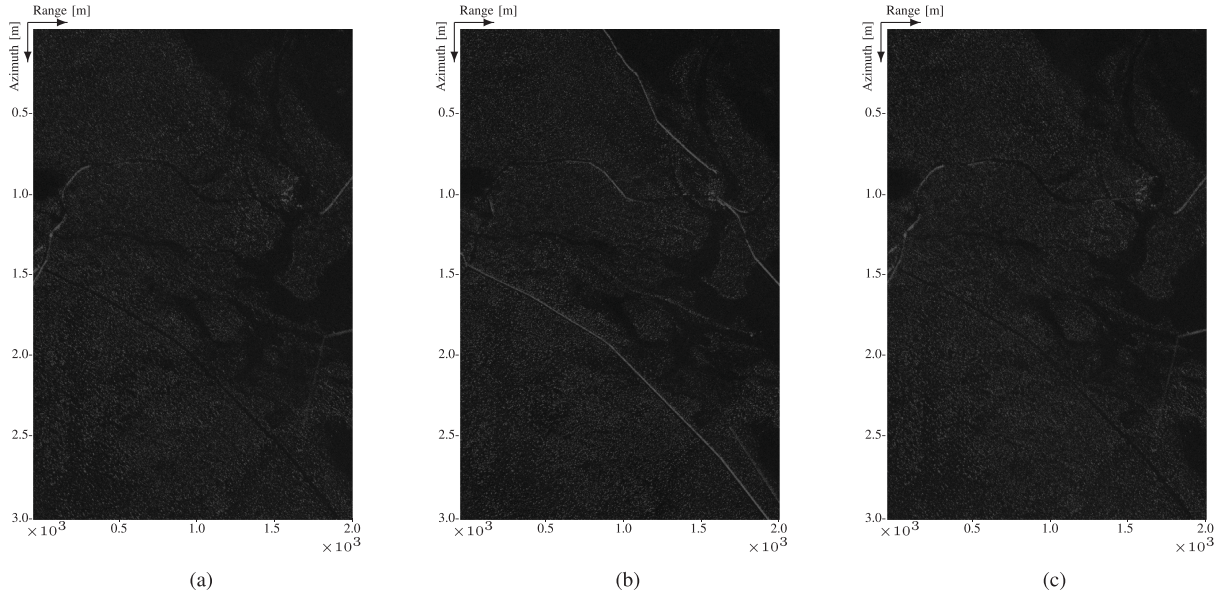


Fig. 5. GSE-RPCA-1 (i.e., interest image) using a stack of CARABAS-II images ($N = 8$): (a) Stack 1; (b) Stack 2; and (c) Stack 3.

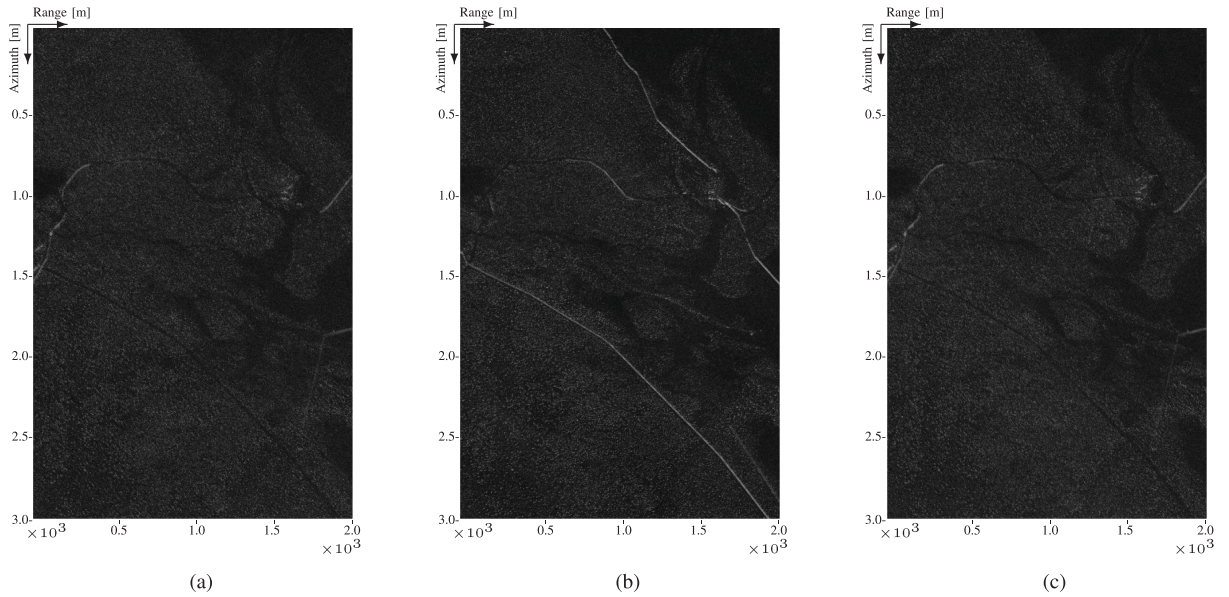


Fig. 6. GSE-TRPCA-1 (i.e., interest image) using a stack of CARABAS-II images ($N = 8$): (a) Stack 1; (b) Stack 2; and (c) Stack 3.

$$\sigma = \sqrt{\frac{1}{Q-1} \sum_{i=1}^Q (x[q] - \bar{x})^2}, \quad (24)$$

$$\mu_3 = \frac{1}{Q} \sum_{q=1}^Q \left(\frac{x[q] - \bar{x}}{\sigma} \right)^3, \quad (25)$$

and

$$\mu_4 = \frac{1}{Q} \sum_{q=1}^Q \left(\frac{x[q] - \bar{x}}{\sigma} \right)^4 \quad (26)$$

where Q represents the total number of pixels ($n \times m$) and $x[q]$ represents the q pixel in the interest image. According to Table II, our method can reduce metrics sensitive to outliers like \bar{x} and σ when compared to [10]. We also obtained a reduction in μ_3 and μ_4 . Outliers due to non-Gaussian signals (such as targets) have high values and appear in the tails of the distribution. As a result, the tails of the distribution are heavier, and μ_3 and μ_4 assume high values that destroy the symmetry of the distribution [71]. It can be concluded that our method is better at replacing targets of the interest image with clutter-plus-noise content than the reference method.

Also, we can assess the performance of GSE methods through numerical error evaluation. The error is calculated by comparing

TABLE II
 \bar{x} , σ , μ_3 , AND μ_4 OF ONE INTEREST IMAGE AND ITS RESPECTIVE GSE USING IMAGE STACKS FROM THE CARABAS-II SYSTEM

Method	\bar{x}	σ	μ_3	μ_4
Stack 1				
Interest Image	0.1442	0.0894	1.8597	14.1740
GSE-RPCA	0.1123	0.0477	1.9552	8.2578
GSE-TRPCA	0.1397	0.0563	1.0693	4.8079
Trimmed mean [10]	0.1430	0.0680	2.9051	21.2919
Median [10]	0.1424	0.0688	2.8231	20.4990
Mean [10]	0.1467	0.0663	3.0516	22.8448
Stack 2				
Interest Image	0.1373	0.0968	2.9345	30.5666
GSE-RPCA	0.1078	0.0530	2.1717	8.8513
GSE-TRPCA	0.1322	0.0619	1.7020	7.6284
Trimmed mean [10]	0.1344	0.0806	4.4488	55.4260
Median [10]	0.1339	0.0812	4.3664	53.9367
Mean [10]	0.1376	0.0792	4.6022	58.3558
Stack 3				
Interest Image	0.1451	0.0905	1.8583	14.0932
GSE-RPCA	0.1122	0.0473	1.7702	7.3178
GSE-TRPCA	0.1401	0.0549	1.0563	4.7661
Trimmed mean [10]	0.1372	0.0665	2.8811	22.0954
Median [10]	0.1366	0.0674	2.8090	21.3242
Mean [10]	0.1410	0.0646	2.9582	22.9540

the pixel amplitude of the interest image and the respective generated GSE. More precisely, the mean square error (MSE), the mean absolute percentage error (MAPE), and the median absolute error (MdAE) were considered [72], [73], [74]. These measures are defined as

$$\text{MSE} = \frac{1}{Q} \sum_{q=1}^Q (x[q] - \hat{x}[q])^2, \quad (27)$$

$$\text{MAPE} = \frac{1}{Q} \sum_{q=1}^Q \frac{|x[q] - \hat{x}[q]|}{|x[q]|}, \quad (28)$$

$$\text{MdAE} = \text{Median}(|x[q] - \hat{x}[q]|) \quad (29)$$

where $\hat{x}[q]$ represents the q pixel in the GSE and $\text{Median}(\cdot)$ represents the central value of a set of ordered values.

Table III presents the quantitative analysis results of the GSE method generated from different stacks, and the best measurements are highlighted. In this analysis, we removed the target region to evaluate our GSE. The target region considered was 100 pixels in range and azimuth from the most extreme target location in the deployment. This strategy was also adopted by [10] and is justified by the fact that the target deployment should not influence the evaluation of the GSE since this content is not expected to be in the GSE. Compared with other methods, the GSE-TRPCA obtains the lowest MSE, MAPE, and MdAE, which indicates that the GSE obtained by our method has the best performance regarding predicting the ground scene among the evaluated techniques. Meanwhile, the GSE-RPCA performed similarly to the reference method with better performance in MAPE, which is a more suitable measure to assess the accuracy of the estimation in different applications [73].

Fig. 7 shows the GSE obtained based on RPCA and TRPCA using WR SAR with $N = 2$. In this case, images from different missions and the same flight heading were considered (Mission

TABLE III
 GSE IMAGE QUALITY MEASURES COMPARED TO REFERENCE USING DATA FROM THE CARABAS-II SYSTEM

Method	MSE	MAPE	MdAE
Stack 1			
GSE-RPCA	0.0052	0.5203	0.0390
GSE-TRPCA	0.0018	0.3584	0.0146
Trimmed mean [10]	0.0037	0.6233	0.0367
Median [10]	0.0037	0.6170	0.0355
Mean [10]	0.0036	0.6537	0.0405
Stack 2			
GSE-RPCA	0.0051	0.5186	0.0352
GSE-TRPCA	0.0022	0.3911	0.0160
Trimmed mean [10]	0.0030	0.6015	0.0329
Median [10]	0.0031	0.5956	0.0318
Mean [10]	0.0030	0.6300	0.0362
Stack 3			
GSE-RPCA	0.0053	0.5095	0.0384
GSE-TRPCA	0.0021	0.3943	0.0175
Trimmed mean [10]	0.0037	0.5852	0.0361
Median [10]	0.0038	0.5794	0.0350
Mean [10]	0.0036	0.6149	0.0395

1 and 2, Pass 1). The reference methods do not work properly when no image stacks are present. On the other hand, our method is able to provide the GSE without the presence of targets, even with few images.

B. GSE Results on PALSAR SAR Images

Fig. 8 shows the interest image [Fig. 3(a)] and the GSE obtained from our model on PALSAR images. In this case, we considered a stack with four images shown in Fig. 3. Based on visual inspection, we can observe that our method manages to remove the ships close to the port region even with a stack formed by only four images, preserving the clutter-plus-noise of the region.

More details about estimation features can be seen in Figs. 9 and 10. These figures represent two regions from Fig. 8 of size 400×400 m (forest and sea regions). The forest region is located in the range $\in [0 \text{ m}, 400 \text{ m}]$ and azimuth $\in [0 \text{ m}, 400 \text{ m}]$, while the sea region is located in the range $\in [1600 \text{ m}, 2000 \text{ m}]$ and azimuth $\in [1200 \text{ m}, 1600 \text{ m}]$. As a result, GSE-TRPCA proved to be a more sensitive estimation method to texture and shading effects than GSE-RPCA. This can be justified because the singular values of tensor data represent important information for shadows and textures. Given that only four images were considered, a loss in this type of information is expected.

Table IV displays the statistical characteristics of the GSE (Fig. 8) in terms of average, standard deviation, skewness, and kurtosis for an image stack. For full-size images, i.e., 6 million pixels per image, the GSE statistics, mainly the GSE-TRPCA, are practically similar to the statistics of the interest image, with no presence of ships for both methods. When we analyze the forest and sea regions, i.e., 160 thousand pixels per image, the methods provided excellent overall performance without significant changes in the statistics of the interest image.

We also evaluated our GSE methods on the PALSAR images regarding MSE, MAPE, and MdAE. Since we do not have access to the ground truth of the targets in the SAR image (e.g., ships close to the port), we evaluated the method in the forest and

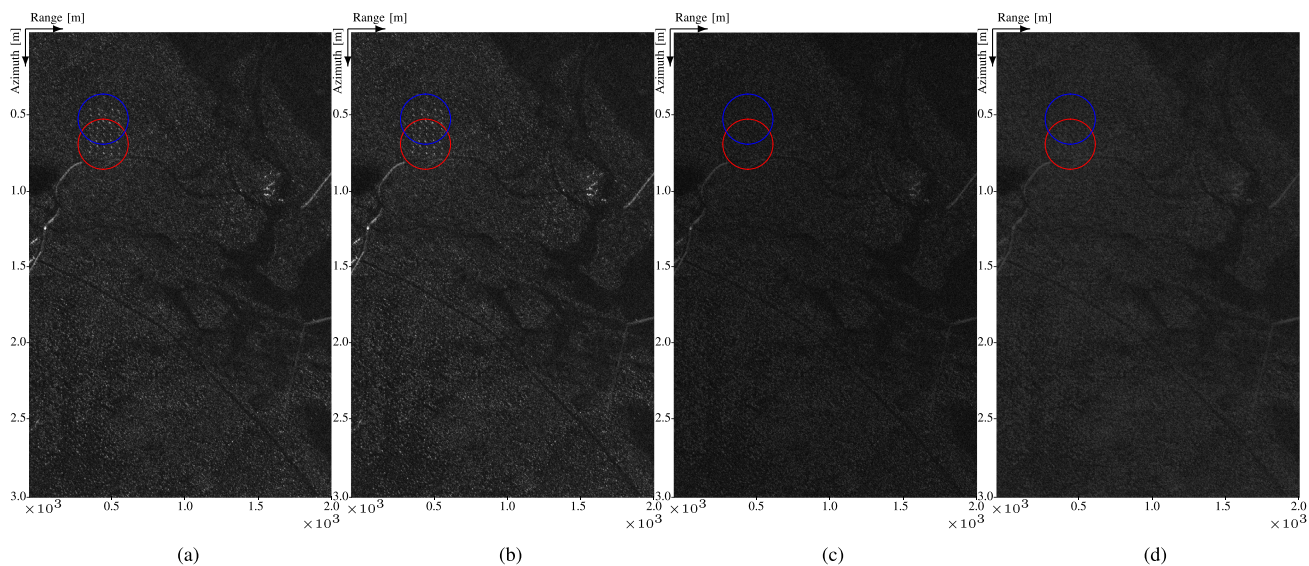


Fig. 7. GSE using pair of SAR images from CARABAS-II system ($N = 2$, Mission 1 and 2, Pass 1). (a) Mean [10]; (b) Median [10]; (c) GSE-RPCA-1; and (d) GSE-TRPCA-1. The areas highlighted by circles in the images represent the regions (two different missions) where the targets are deployed.

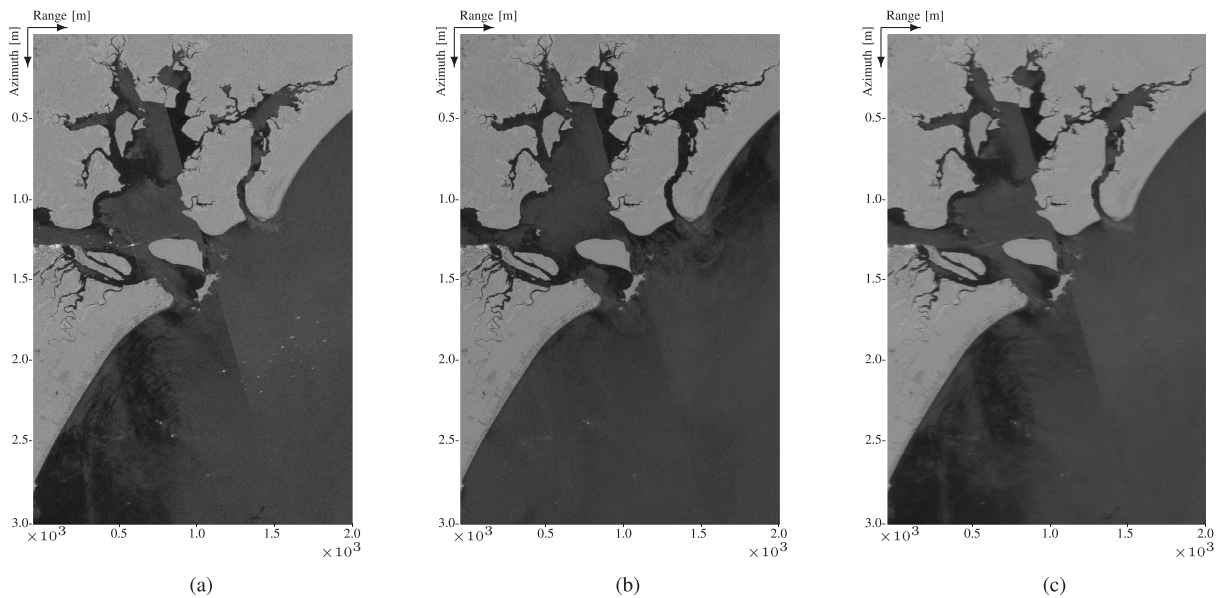


Fig. 8. GSE using four PALSAR images ($N = 4$, Fig. 3). (a) Interest image; (b) GSE-RPCA of (a); (c) GSE-TRPCA of (a).

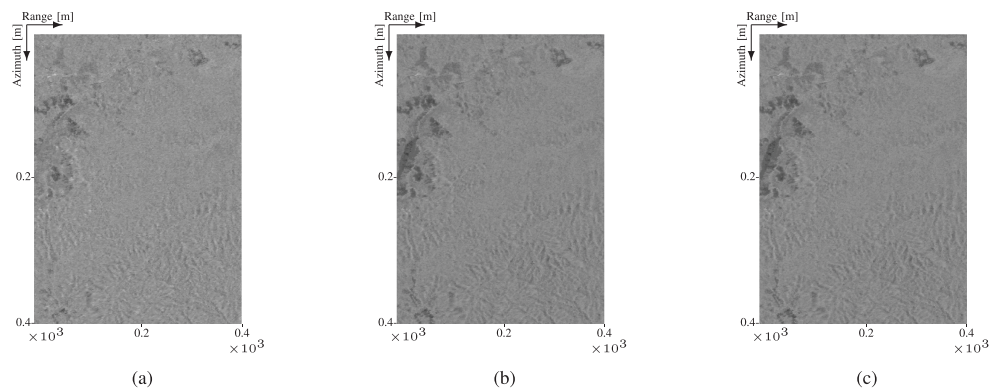


Fig. 9. Forest region-GSE using four PALSAR images ($N = 4$, Fig. 3). (a) Interest image; (b) GSE-RPCA of (a); (c) GSE-TRPCA of (a).

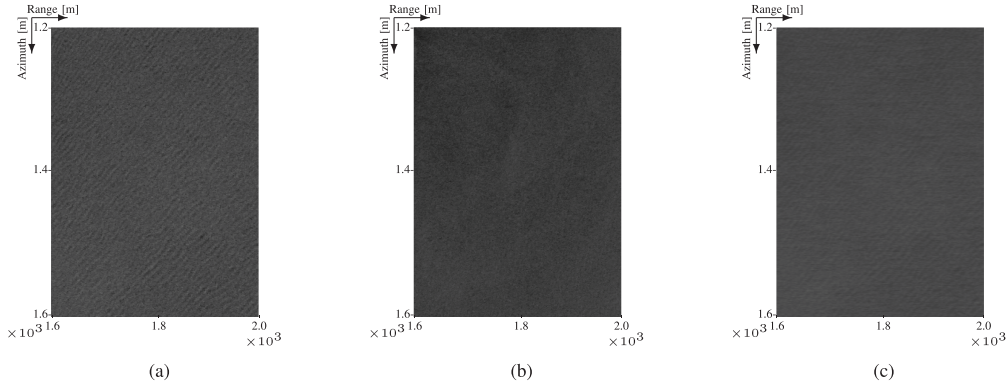


Fig. 10. Sea region-GSE using four PALSAR images ($N = 4$, Fig. 3). (a) Interest image; (b) GSE-RPCA of (a); (c) GSE-TRPCA of (a).

TABLE IV

AVERAGE, STANDARD DEVIATION, SKEWNESS, AND KURTOSIS OF AN INTEREST IMAGE, A FOREST REGION, AND A SEA REGION AND THE RESPECTIVE GSE USING IMAGE STACK FROM THE PALSAR SYSTEM

Data	\bar{x}	σ	μ_3	μ_4
Interest Image – Fig. 3(a)				
Full size	0.3618	0.1689	0.3367	1.5600
Forest	0.5629	0.0432	-0.7635	5.6742
Sea	0.2867	0.0303	-0.1523	3.1528
GSE-RPCA				
Full size	0.3410	0.1547	0.4361	1.5007
Forest	0.5272	0.0408	-1.1334	5.6812
Sea	0.2331	0.0278	-0.4656	3.4582
GSE-TRPCA				
Full size	0.3621	0.1626	0.3399	1.4464
Forest	0.5628	0.0234	-1.4367	8.3373
Sea	0.2879	0.0147	0.2273	3.7218

TABLE V
GSE IMAGE QUALITY MEASURES USING PALSAR DATA

Method	MSE		MAPE		MdAE	
	Forest	Sea	Forest	Sea	Forest	Sea
Interest Image – Fig. 3(a)						
GSE-RPCA	0.0024	0.0042	0.0621	0.1825	0.0301	0.0517
GSE-TRPCA	0.0009	0.0005	0.0369	0.0587	0.0143	0.0116
Interest Image – Fig. 3(b)						
GSE-RPCA	0.0020	0.0013	0.0548	0.1276	0.0245	0.0143
GSE-TRPCA	0.0010	0.0006	0.0403	0.0873	0.0151	0.0122
Interest Image – Fig. 3(c)						
GSE-RPCA	0.0023	0.0010	0.0609	0.1033	0.0273	0.0036
GSE-TRPCA	0.0009	0.0005	0.0393	0.0798	0.0150	0.0112
Interest Image – Fig. 3(d)						
GSE-RPCA	0.0017	0.0028	0.0508	0.1441	0.0206	0.0356
GSE-TRPCA	0.0009	0.0005	0.0392	0.0598	0.0144	0.0109

sea clutter-plus-noise regions, previously presented in Figs. 9 and 10, respectively. Table V shows the error measures between the image of interest and the respective GSE obtained. Similar to the results presented with WR SAR images, the GSE-TRPCA method performed better than the GSE-RPCA in the PALSAR data, confirming the robustness of the method. Furthermore, our methods proved efficient in predicting the ground in a scene formed by different types of clutter-plus-noise (e.g., forest and sea).

C. Discussion

Using λ_{RPCA} defined in (4), the rank of \mathbf{L} is equal to 1 in all scenarios, which means that in a stack with N images, GSE-RPCA provides N GSE's where all estimation are linearly dependent. This feature implies that the GSE-RPCA obtains a single GSE since one GSE is just a linear combination of any other GSE of the stack. On the other hand, the rank of \mathcal{L} is equal to N in all scenarios. Therefore, the GSE-TRPCA provides N linearly independent GSE for the stack. Our method shows that a single GSE can represent very well the clutter-plus-noise of the whole stack formed by SAR images from the same flight heading. However, strategies that allow linearly independent GSEs are more efficient, as observed in Table III.

It is interesting to observe how each method obtains the GSE. As a matrix solution, the GSE-RPCA has become less sensitive to texture and shading effects. This is because when vectorizing each image to organize \mathbf{X} , part of the spatial information is lost while the temporal information is preserved. On the other hand, GSE-TRPCA, being a tensor method that considers all spatial information contained in the stack, eliminates the texture and shadow information from the GSE until a convergence criterion is reached.

However, since statistical characteristics of the GSE depend on λ choice, future works may seek to optimize this value, providing more texture and shadow information to the GSE and, consequently, increasing the performance of the method. Another way to improve estimation performance is to increase the number of images in the stack with noise or targets. If the noise from the added images behaves similarly to the other noise already present in the stack, this behavior will help the method to obtain an accurate estimation. If this noise differs from the other images, it tends to be represented by the sparse matrix and not in the GSE. Adding images with outliers will also help the GSE method, as this type of content is often sparse as a whole in the data.

Regarding the runtime processing, the methods were implemented on a computer equipped with an Intel Core i7-7700 processor with a 3.6 GHz CPU, 16 GB memory, an Intel HD Graphics 630, and the requisite software environment is the MATLAB R2021a. The average runtime processing and standard deviation

TABLE VI
RUNNING TIME COMPARISON FOR THE GSE METHODS

System	Data	N	Method	$\bar{x} \pm \sigma$ (s)
CARABAS-II	Stack 1	8	GSE-RPCA	118.8285 ± 0.2351
			GSE-TRPCA	276.3218 ± 1.8462
	Stack 2	8	GSE-RPCA	118.8230 ± 0.1950
			GSE-TRPCA	305.4330 ± 0.7333
	Stack 3	8	GSE-RPCA	118.8664 ± 0.2640
			GSE-TRPCA	275.3143 ± 1.7744
PALSAR	Stack	4	GSE-RPCA	36.7970 ± 0.2394
			GSE-TRPCA	122.3717 ± 0.2233
	Pair	2	GSE-RPCA	11.2508 ± 0.0294
			GSE-TRPCA	65.9217 ± 0.1674

of the GSE methods are presented in Table VI. These values were obtained considering 10 simulations with SAR images of size 3000×2000 . It is worth noting that the proposed method, either matrix or tensor solution, does not depend on other steps, such as a training step, which can significantly reduce the algorithm runtime processing.

Finally, it is understood that the complexity of the proposed method depends on the optimization process. Based on the ADMM method, the complexity of the RPCA via PCP is equal to $\mathcal{O}(n_1 n_2 \min(n_1, n_2))$ [20] and the complexity of the TRPCA via TNN is equal to $\mathcal{O}(n_1 n_2 n_3 \log n_3 + n_1 n_2^2 n_3)$ [35]. Considering the GSE methodology, the complexity of the GSE-RPCA and the GSE-TRPCA is equal to $\mathcal{O}(N^2 nm)$ and $\mathcal{O}(N^2 nm(\frac{\log m}{N} + n))$, respectively.

V. CONCLUSION

Obtaining the GSE in SAR imagery is a challenge. This article proposes a GSE method through robust PCA techniques based on matricial and tensorial formulations. The amount of information presented in both proposed GSE methods is based on a single regularization parameter, which depends only on the dimensions of the input data. In addition, the proposed method has another attractive characteristic, i.e., it works for any size of SAR image stack. Experiments based on wavelength-resolution SAR images from the CARABAS-II system and polarimetric SAR images from the ALOS PALSAR system showed that the proposed method provides a good quality GSE for different scenes. We evaluated the proposed method based on visual inspection, statistical characteristics, and quality adjustment measures. In this context, our method produced the most reliable estimation compared to the state-of-the-art reference method.

Unlike strategies that use pixel-by-pixel analysis, robust PCA techniques are not sensitive to outliers missing data and do not require data training steps, which makes GSE solutions based on robust PCA techniques applicable for different types of SAR systems. Finally, this article proposes two robust GSE methods that decompose data into L+S. In future work, other recent formulations can be investigated [23]. In addition, the GSE problem can be explored based on other matrix/tensor factorization techniques, such as nonnegative matrix factorization (NNMF), among others [75].

TABLE VII
LIST OF ACRONYMS AND ABBREVIATIONS

Symbol	Description
ADMM	Alternating Direction Method of Multiplier
AFRL	U.S. Air Force Research Laboratory
ALM	Augmented Lagrange Multiplier
ALOS	Advanced Land Observing Satellite
CARABAS	Coherent All Radio Band System
FOA	Swedish National Defence Research Establishment
GMTI	Ground Moving-Target Indication
GSE	Ground Scene Estimation
GSE-RPCA	Ground Scene Estimation from RPCA
GSE-TRPCA	Ground Scene Estimation from TRPCA
JAXA	Japan Aerospace Exploration Agency
NNMF	Non-negative Matrix Factorization
MAPE	Mean Absolute Percentage Error
MdAE	Median Absolute Error
MSE	Mean Square Error
PALSAR	Phased Arrayed L-band Synthetic Aperture Radar
PCA	Principal Component Analysis
PCP	Principal Component Pursuit
RPCA	Robust Principal Component Analysis
SAR	Synthetic Aperture Radar
SDMS	Sensor Data Management System
TNN	Tensor Nuclear Norm
TRPCA	Tensor Robust Principal Component Analysis
UWB	Ultra-wideband
VHF	Very-high frequency
WR	Wavelength-Resolution

APPENDIX A

ACRONYMS AND ABBREVIATIONS

In Table VII, we provide a list of acronyms and abbreviations used in this work.

REFERENCES

- [1] A. Moreira, P. Prats-Iraola, M. Younis, G. Krieger, I. Hajnsek, and K. P. Papathanassiou, "A tutorial on synthetic aperture radar," *IEEE Geosci. Remote Sens. Mag.*, vol. 1, no. 1, pp. 6–43, Mar. 2013.
- [2] E. Rignot et al., "Recent antarctic ice mass loss from radar interferometry and regional climate modeling," *Nature Geosci.*, vol. 1, no. 2, pp. 106–110, 2008.
- [3] A. Moreira et al., "Tandem-L: A highly innovative bistatic SAR mission for global observation of dynamic processes on the Earth's surface," *IEEE Geosci. Remote Sens. Mag.*, vol. 3, no. 2, pp. 8–23, Jun. 2015.
- [4] R. Seu, S. Smrekar, S. Hensley, and P. Lombardo, "A SAR interferometer experiment to explore the surface of venus," in *Proc. EUSAR: 11th Eur. Conf. Synthetic Aperture Radar*, 2016, pp. 1–3.
- [5] L. M. Ulander, W. E. Pierson, M. Lundberg, P. Follo, P.-O. Frolind, and A. Gustavsson, "Performance of VHF-band SAR change detection for wide-area surveillance of concealed ground targets," in *Proc. SPIE Conf. Algorithms Synthetic Aperture Radar Imagery*, 2004, vol. 5427, pp. 259–270.
- [6] L. M. Ulander, M. Lundberg, W. Pierson, and A. Gustavsson, "Change detection for low-frequency SAR ground surveillance," *IEE Proc.-Radar, Sonar, Navigation*, vol. 152, no. 6, pp. 413–420, 2005.
- [7] A. Asokan and J. Anitha, "Change detection techniques for remote sensing applications: A survey," *Earth Sci. Informat.*, vol. 12, no. 2, pp. 143–160, 2019.
- [8] D. Hammett, "A study of clutter reduction techniques in wide bandwidth HF/VHF deep ground penetrating radar," M.S. thesis, Rochester Inst. of Technol., Rochester, NY, USA, 2002.
- [9] L. P. Ramos, R. F. Da Costa, D. D. S. De Medeiros, P. R. B. Da Silva, D. I. Alves, and R. Machado, "On the effect of imperfect reference images in SAR change detection based on Bayes' theorem," in *Proc. XL Braz. Symp. Telecommun. Signal Process.*, 2022, pp. 1–5.
- [10] B. G. Palm et al., "Wavelength-resolution SAR ground scene prediction based on image stack," *Sensors*, vol. 20, no. 7, 2020, Art. no. 2008.
- [11] D. I. Alves et al., "Wavelength-resolution SAR change detection using Bayes' theorem," *IEEE J. Sel. Topics Appl. Earth Observ. Remote Sens.*, vol. 13, pp. 5560–5568, 2020.

- [12] D. I. Alves et al., "Change detection method for wavelength-resolution SAR images based on Bayes' theorem: An iterative approach," *IEEE Access*, vol. 11, pp. 84734–84743, 2023.
- [13] G. Gao, "Statistical modeling of SAR images: A survey," *Sensors*, vol. 10, no. 1, pp. 775–795, 2010.
- [14] D.-X. Yue, F. Xu, A. C. Frery, and Y.-Q. Jin, "Synthetic aperture radar image statistical modeling: Part one-single-pixel statistical models," *IEEE Geosci. Remote Sens. Mag.*, vol. 9, no. 1, pp. 82–114, Mar. 2020.
- [15] V. T. Vu, M. I. Pettersson, R. Machado, P. Dammert, and H. Hellsten, "False alarm reduction in wavelength-resolution SAR change detection using adaptive noise canceler," *IEEE Trans. Geosci. Remote Sens.*, vol. 55, no. 1, pp. 591–599, Jan. 2017.
- [16] N. R. Gomes, P. Dammert, M. I. Pettersson, V. T. Vu, and H. Hellsten, "Comparison of the Rayleigh and K-distributions for application in incoherent change detection," *IEEE Geosci. Remote Sens. Lett.*, vol. 16, no. 5, pp. 756–760, May 2019.
- [17] B. G. Palm, F. M. Bayer, R. J. Cintra, M. I. Pettersson, and R. Machado, "Rayleigh regression model for ground type detection in SAR imagery," *IEEE Geosci. Remote Sens. Lett.*, vol. 16, no. 10, pp. 1660–1664, Oct. 2019.
- [18] B. G. Palm et al., "Autoregressive model for multi-pass SAR change detection based on image stacks," in *Proc. Image Signal Process. Remote Sens.*, 2018, vol. 10789, Art. no. 1078916.
- [19] G. R. Naik et al. *Blind Source Separation*, vol. 10. Berlin, Germany: Springer, 2014, pp. 978–983.
- [20] T. Bouwmans and E. H. Zahzah, "Robust PCA via principal component pursuit: A review for a comparative evaluation in video surveillance," *Comput. Vis. Image Understanding*, vol. 122, pp. 22–34, 2014.
- [21] E. J. Candès, X. Li, Y. Ma, and J. Wright, "Robust principal component analysis?," *J. ACM*, vol. 58, no. 3, pp. 1–37, 2011.
- [22] T. Bouwmans, S. Javed, H. Zhang, Z. Lin, and R. Otazo, "On the applications of robust PCA in image and video processing," *Proc. IEEE*, vol. 106, no. 8, pp. 1427–1457, Aug. 2018.
- [23] N. Vaswani, T. Bouwmans, S. Javed, and P. Narayanamurthy, "Robust subspace learning: Robust PCA, robust subspace tracking, and robust subspace recovery," *IEEE Signal Process. Mag.*, vol. 35, no. 4, pp. 32–55, Jul. 2018.
- [24] H. Yan, R. Wang, F. Li, Y. Deng, and Y. Liu, "Ground moving target extraction in a multichannel wide-area surveillance SAR/GMTI system via the relaxed PCP," *IEEE Geosci. Remote Sens. Lett.*, vol. 10, no. 3, pp. 617–621, May 2013.
- [25] A. H. Oveis and M. A. Sebt, "Dictionary-based principal component analysis for ground moving target indication by synthetic aperture radar," *IEEE Geosci. Remote Sens. Lett.*, vol. 14, no. 9, pp. 1594–1598, Sep. 2017.
- [26] S. Thammakhoune, B. Yonel, E. Mason, B. Yazici, and Y. C. Eldar, "Moving target imaging for synthetic aperture radar via RPCA," in *Proc. IEEE Radar Conf.*, 2021, pp. 1–6.
- [27] C. Schwartz et al., "Change detection in UWB SAR images based on robust principal component analysis," *Remote Sens.*, vol. 12, no. 12, 2020, Art. no. 1916.
- [28] L. P. Ramos et al., "A wavelength-resolution SAR change detection method based on image stack through robust principal component analysis," *Remote Sens.*, vol. 13, no. 5, 2021, Art. no. 833.
- [29] M. Gong, Y. Li, L. Jiao, M. Jia, and L. Su, "SAR change detection based on intensity and texture changes," *ISPRS J. Photogrammetry Remote Sens.*, vol. 93, pp. 123–135, 2014.
- [30] D. Yang, X. Yang, G. Liao, and S. Zhu, "Strong clutter suppression via RPCA in multichannel SAR/GMTI system," *IEEE Geosci. Remote Sens. Lett.*, vol. 12, no. 11, pp. 2237–2241, Nov. 2015.
- [31] S. Song and J. Yang, "Ship detection in polarimetric SAR images via tensor robust principle component analysis," in *Proc. Int. Geosci. Remote Sens. Symp.*, 2015, pp. 3152–3155.
- [32] C. Lu, J. Feng, Y. Chen, W. Liu, Z. Lin, and S. Yan, "Tensor robust principal component analysis: Exact recovery of corrupted low-rank tensors via convex optimization," in *Proc. IEEE Conf. Comput. Vis. Pattern Recognit.*, 2016, pp. 5249–5257.
- [33] J. Kang, Y. Wang, M. Schmitt, and X. X. Zhu, "Object-based multipass InSAR via robust low-rank tensor decomposition," *IEEE Trans. Geosci. Remote Sens.*, vol. 56, no. 6, pp. 3062–3077, Jun. 2018.
- [34] W. Sun, G. Yang, J. Peng, and Q. Du, "Lateral-slice sparse tensor robust principal component analysis for hyperspectral image classification," *IEEE Geosci. Remote Sens. Lett.*, vol. 17, no. 1, pp. 107–111, Jan. 2020.
- [35] C. Lu, J. Feng, Y. Chen, W. Liu, Z. Lin, and S. Yan, "Tensor robust principal component analysis with a new tensor nuclear norm," *IEEE Trans. Pattern Anal. Mach. Intell.*, vol. 42, no. 4, pp. 925–938, Apr. 2020.
- [36] L. Ulander et al., "Performance of the CARABAS-II VHF-band synthetic aperture radar," in *Proc. Scanning Present Resolving Future, IEEE Int. Geosci. Remote Sens. Symp.*, 2001, vol. 1, pp. 129–131.
- [37] A. Gustavsson et al., "Development and operation of an airborne VHF SAR system-lessons learned," in *Proc. Sens. Manag. Environ., IEEE Int. Geosci. Remote Sens. Symp.*, 1998, vol. 1, pp. 458–462.
- [38] T. G. Bryant, G. B. Morse, L. M. Novak, and J. C. Henry, "Tactical radars for ground surveillance," *Lincoln Lab. J.*, vol. 12, no. 2, pp. 341–354, 2000.
- [39] H. Hellsten, L. M. Ulander, A. Gustavsson, and B. Larsson, "Development of VHF CARABAS II SAR," in *Proc. Int. Conf. SPIE Radar Sensor Technol.*, 1996, vol. 2747, pp. 48–60.
- [40] M. Lundberg, L. M. Ulander, W. E. Pierson, and A. Gustavsson, "A challenge problem for detection of targets in foliage," in *Proc. Conf. SPIE Algorithms Synthetic Aperture Radar Imagery*, 2006, vol. 6237, pp. 160–171.
- [41] U.S. Air Force, "The sensor data management system," Accessed on: May 3, 2022. [Online]. Available: <https://www.sdms.afrl.af.mil>
- [42] J.-S. Lee and E. Pottier, *Polarimetric Radar Imaging: From Basics to Applications*. Boca Raton, FL, USA: CRC Press, 2017.
- [43] M. Shimada et al., "New global forest/non-forest maps from ALOS PALSAR data (2007–2010)," *Remote Sens. Environ.*, vol. 155, pp. 13–31, 2014.
- [44] Japan Aerospace Exploration Agency, "Earth observation research center," Accessed on: Aug. 3, 2022. [Online]. Available: https://www.eorc.jaxa.jp/ALOS/en/index_e.htm
- [45] M. Shimada, O. Isoguchi, T. Tadono, and K. Isono, "PALSAR radiometric and geometric calibration," *IEEE Trans. Geosci. Remote Sens.*, vol. 47, no. 12, pp. 3915–3932, Dec. 2009.
- [46] I. T. Jolliffe and J. Cadima, "Principal component analysis: A review and recent developments," *Philos. Trans. Roy. Soc. A: Mathe., Phys. Eng. Sci.*, vol. 374, no. 2065, 2016, Art. no. 20150202.
- [47] N. Vaswani and P. Narayanamurthy, "Static and dynamic robust PCA and matrix completion: A review," *Proc. IEEE*, vol. 106, no. 8, pp. 1359–1379, Aug. 2018.
- [48] L. C. Lee and A. A. Jemain, "On overview of PCA application strategy in processing high dimensionality forensic data," *Microchem. J.*, vol. 169, 2021, Art. no. 106608.
- [49] M. Udell et al., "Generalized low-rank models," *Found. Trends Mach. Learn.*, vol. 9, no. 1, pp. 1–118, 2016.
- [50] J. Feng, H. Xu, and S. Yan, "Robust PCA in high-dimension: A deterministic approach," in *Proc. Int. Conf. Mach. Learn.*, Edinburgh, Scotland, 2012, pp. 1827–1834.
- [51] S. Serneels and T. Verdonck, "Principal component analysis for data containing outliers and missing elements," *Comput. Statist. Data Anal.*, vol. 52, no. 3, pp. 1712–1727, 2008.
- [52] P. Comon and C. Jutten, *Handbook of Blind Source Separation: Independent Component Analysis and Applications*. New York, NY, USA: Academic Press, 2010.
- [53] Z. Lin, M. Chen, and Y. Ma, "The augmented Lagrange multiplier method for exact recovery of corrupted low-rank matrices," UIUC, Tech. Rep. UILU-ENG-09-2215, 2009.
- [54] G. Liu et al., "Robust subspace segmentation by low-rank representation," in *Proc. Int. Conf. Mach. Learn.*, 2010, vol. 1, Art. no. 8.
- [55] S. Boyd et al., "Distributed optimization and statistical learning via the alternating direction method of multipliers," *Found. Trends Mach. Learn.*, vol. 3, no. 1, pp. 1–122, 2011.
- [56] S. Bartels and M. Milicevic, "Alternating direction method of multipliers with variable step sizes," 2017, [arXiv:1704.06069](https://arxiv.org/abs/1704.06069).
- [57] J.-F. Cai, E. J. Candès, and Z. Shen, "A singular value thresholding algorithm for matrix completion," *SIAM J. Optim.*, vol. 20, no. 4, pp. 1956–1982, 2010.
- [58] J. Wicker, B. Pfahringer, and S. Kramer, "Multi-label classification using boolean matrix decomposition," in *Proc. 27th Annu. ACM Symp. Appl. Comput.*, 2012, pp. 179–186.
- [59] B. Karan, S. S. Sahu, J. R. Orozco-Arroyave, and K. Mahto, "Non-negative matrix factorization-based time-frequency feature extraction of voice signal for Parkinson's disease prediction," *Comput. Speech Lang.*, vol. 69, 2021, Art. no. 101216.
- [60] A. Cichocki et al., "Tensor decompositions for signal processing applications: From two-way to multiway component analysis," *IEEE Signal Process. Mag.*, vol. 32, no. 2, pp. 145–163, Mar. 2015.
- [61] M. Mørup, "Applications of tensor (multiway array) factorizations and decompositions in data mining," *Wiley Interdiscipl. Rev.: Data Mining Knowl. Discov.*, vol. 1, no. 1, pp. 24–40, 2011.
- [62] Z. Zhang, G. Ely, S. Aeron, N. Hao, and M. Kilmer, "Novel methods for multilinear data completion and de-noising based on tensor-SVD," in *Proc. IEEE Conf. Comput. Vis. Pattern Recognit.*, 2014, pp. 3842–3849.

- [63] X.-L. Zhao, W.-H. Xu, T.-X. Jiang, Y. Wang, and M. K. Ng, "Deep plug-and-play prior for low-rank tensor completion," *Neurocomputing*, vol. 400, pp. 137–149, 2020.
- [64] M. E. Kilmer and C. D. Martin, "Factorization strategies for third-order tensors," *Linear Algebra Appl.*, vol. 435, no. 3, pp. 641–658, 2011.
- [65] L. Feng, Y. Liu, L. Chen, X. Zhang, and C. Zhu, "Robust block tensor principal component analysis," *Signal Process.*, vol. 166, 2020, Art. no. 107271.
- [66] D. Laptev, "PCA robust," Accessed on: Jul. 3, 2022. [Online]. Available: <https://github.com/dlaptev/RobustPCA>
- [67] C. Lu, "Tensor robust PCA," Accessed on: Oct. 3, 2022. [Online]. Available: <https://github.com/canyilu/Tensor-Robust-Principal-Component-Analysis-TRPCA>
- [68] R. Machado, V. T. Vu, M. I. Pettersson, P. Dammert, and H. Hellsten, "The stability of UWB low-frequency SAR images," *IEEE Geosci. Remote Sens. Lett.*, vol. 13, no. 8, pp. 1114–1118, Aug. 2016.
- [69] R. Shanmugam and R. Chatterjee, *Statistics for Scientists and Engineers*. Hoboken, NJ, USA: Wiley, 2015.
- [70] R. A. Maronna, R. D. Martin, V. J. Yohai, and M. Salibián-Barrera, *Robust Statistics: Theory and Methods (With R)*. Hoboken, NJ, USA: Wiley, 2019.
- [71] C. D. Saragiotis, L. J. Hadjileontiadis, and S. M. Panas, "PAI-S/K: A robust automatic seismic P phase arrival identification scheme," *IEEE Trans. Geosci. Remote Sens.*, vol. 40, no. 6, pp. 1395–1404, Jun. 2002.
- [72] C. Chatfield, *Time-Series Forecasting*. London, U.K.: Chapman and Hall/CRC, 2000.
- [73] R. J. Hyndman and A. B. Koehler, "Another look at measures of forecast accuracy," *Int. J. Forecasting*, vol. 22, no. 4, pp. 679–688, 2006.
- [74] D. Koutsandreas, E. Spiliotis, F. Petropoulos, and V. Assimakopoulos, "On the selection of forecasting accuracy measures," *J. Oper. Res. Soc.*, vol. 73, no. 5, pp. 937–954, 2022.
- [75] A. Sobral, T. Bouwmans, and E. Zahzah, "LRSLibrary: Low-rank and sparse tools for background modeling and subtraction in videos," Accessed on: May 12, 2023. [Online]. Available: <https://github.com/andrewssobral/lrslibrary>



Lucas P. Ramos (Student Member, IEEE) received the B.S.E.E degree from the Federal University of Pampa (UNIPAMPA), Alegrete, Brazil, in 2019, and the M.Sc. degree in electronics and computer engineering, in 2021 from the Aeronautics Institute of Technology (ITA), São José dos Campos, Brazil, where he is currently working toward the Ph.D. degree in electronics and computer engineering (telecommunications).

He is currently a Visiting Ph.D. student with the Department of Mathematics and Natural Sciences, Blekinge Institute of Technology (BTH), Karlskrona, Sweden. His research interests include image processing and change detection in applications that cover areas of knowledge such as remote sensing and synthetic aperture radar (SAR).

Mr. Ramos's master's dissertation was the recipient of the Cecchini Award for Best Defended Dissertation in 2021 from ITA.



Dimas I. Alves (Member, IEEE) received the B.S.E.E degree from the Federal University of Santa Maria (UFSM), Santa Maria, RS, Brazil, in 2013, and the M.Sc. and the Ph.D. degrees in electrical engineering from the Federal University of Santa Catarina (UFSC), Florianópolis, SC, Brazil, in 2015 and 2020, respectively.

From 2018 to 2019, he was a Visiting Ph.D. Researcher Fellow with the Blekinge Institute of Technology (BTH), Karlskrona, Sweden. Between 2015 and 2021, he was a Professor with the Federal University of Pampa (Unipampa), Alegrete, RS, Brazil. Since 2021, he has been a Professor with the Department of Telecommunications, Aeronautics Institute of Technology and the Graduate Program in electronics and computer engineering (PGEEC), ITA, São José dos Campos, SP, Brazil. His research interests include radars, SAR systems, image processing, and digital signal processing.



Leonardo T. Duarte (Senior Member, IEEE) received the B.S. and M.Sc. degrees in electrical engineering from the University of Campinas (UNICAMP), Campinas, Brazil, in 2004 and 2006, respectively, and the Ph.D. degree from the Grenoble Institute of Technology, Grenoble INP, Université Grenoble Alpes, France, in 2009.

Since 2011, he has been with the School of Applied Sciences (FCA), UNICAMP, Limeira, Brazil, where he is currently an Associate Professor. In 2016, he was a Visiting Professor with the École de Génie Industriel, GI-Grenoble INP, Grenoble, France, and, in 2023, he was a Visiting Professor with the Université de Toulouse III Paul Sabatier, Toulouse, France. His research interests include data science and lie primarily in the fields of signal processing, decision aiding and machine learning, and also in the interplays between these fields.

In 2022, he was elected Affiliated Member (up to 40 years old) of the Brazilian Academy of Sciences (ABC).



Mats I. Pettersson (Senior Member, IEEE) received the M.Sc. degree in engineering physics, the licentiate degree in radio and space science, and the Ph.D. degree in signal processing from the Chalmers University of Technology, Gothenburg, Sweden, in 1993, 1995, and 2000, respectively.

He was with Mobile Communication Research, Ericsson, Lund, Sweden, and with the Swedish Defense Research Agency (FOI) for ten years in Linköping. He focused on ultrawideband low-frequency Synthetic Aperture Radar (SAR) systems at FOI. Since 2005, he has been with the Blekinge Institute of Technology (BTH), Karlskrona, Sweden, where he is a Full Professor. He has authored or coauthored more than 250 scientific publications, of which more than 70 are in peer reviewed scientific journals. His research is related to radar surveillance and remote sensing. His main research interests include SAR processing, space–time adaptive processing (STAP), high-resolution SAR change detection, automotive radar, radio occultation, THz SAR, and computer vision.



Renato Machado (Senior Member, IEEE) was born in Jaú, SP, Brazil, in 1979. He received the B.S.E.E. degree from São Paulo State University (UNESP), Ilha Solteira, SP, Brazil, in 2001, and the master's and Ph.D. degrees in electrical engineering from the Federal University of Santa Catarina (UFSC), Florianópolis, SC, Brazil, in 2004 and 2008, respectively.

From 2006 to 2007, he was a Visiting Ph.D. Scholar with the Department of Electrical Engineering, Arizona State University (ASU), Tempe, AZ, USA. From 2013 to 2015, he was a Visiting Research Fellow with the Blekinge Institute of Technology (BTH), Karlskrona, Sweden, in partnership with Saab AB, Sweden. From August 2009 to December 2017, he was an Assistant Professor (2009–2016) and an Associate Professor (2017) with the Federal University of Santa Maria, RS, Brazil, where he lectured many courses in Bachelor and Graduate Programs and assumed different positions in the institution, namely, the Research Leader of the Communications and Signal Processing Research Group, the Coordinator of the Telecommunications Engineering Program, and the Director of the Aerospace Science Laboratory. Since 2017, he has been an Associate Professor with the Aeronautics Institute of Technology (ITA), São José dos Campos, SP, Brazil. He is also the Research Leader with the Digital and Signal Processing Laboratory and SAR and Radar Signal Processing Laboratory, ITA, and the Head of the Division of Electronic Engineering. His research interests include synthetic aperture radar (SAR) processing, SAR image processing, change detection, radar signal processing, wireless communications, digital signal processing, and AI for signal processing.